Numerical Simulation of the Flow in a Turbopump Inducer in Non-Cavitating and Cavitating Conditions

M. Bilanceri, F. Beux, and M.V. Salvetti

Abstract A numerical methodology for the simulation of cavitating flows in real complex geometries is presented. A homogeneous-flow cavitation model, accounting for thermal effects and active nuclei concentration, which leads to a barotropic state law is adopted. The continuity and momentum equations are discretized through a mixed finite-element/finite-volume approach, applicable to unstructured grids. A robust preconditioned low-diffusive HLL scheme is used to deal with all speed barotropic flows. Second-order accuracy in space is obtained through MUSCL reconstruction. Time advancing is carried out by a second-order implicit linearized formulation together with the Defect Correction technique. The flow in a real 3D inducer for rockets turbopumps is simulated for a wide range of conditions: different flow rates and rotating speeds as well as non-cavitating and cavitating flows are considered. The results obtained with this numerical approach are compared with experimental data.

Keywords cavitating flows, homogeneous flow model, low diffusive HLL scheme, linearized implicit time advancing
MSC2010: 65-06

1 Introduction

A tool for numerical simulation of 3D compressible flows satisfying a barotropic equation of state is presented in this work. In particular, we are interested in simulating cavitating flows through the barotropic homogeneous flow model proposed in [1]. The numerical method used in this work is based on a mixed

---

M. Bilanceri and M.V. Salvetti
University of Pisa (Italy), e-mail: marco.bilanceri@gmail.com, mv.salvetti@ing.unipi.it

F. Beux
Alta S.p.A., Pisa (Italy), e-mail: f.beux@alta-space.com

J. Fořt et al. (eds.), *Finite Volumes for Complex Applications VI – Problems & Perspectives*, Springer Proceedings in Mathematics 4,
DOI 10.1007/978-3-642-20671-9_15,

finite-element/finite-volume spatial discretization on 3D unstructured grids. Viscous fluxes are discretized using P1 finite-elements while for the convective fluxes the LD-HLL scheme [2], a low-diffusive modification of the Rusanov scheme, is adopted. Second-order in space is obtained using a MUSCL reconstruction technique and time-consistent preconditioning is introduced to deal with the low Mach number regime. A linearized implicit time-advancing is associated to a defect-correction technique to obtain a second-order accurate (both in time and space) formulation at a limited computational cost. A non inertial reference frame, rotating at constant angular velocity, is used to account for possible solid-body rotation and the standard $k - \varepsilon$ turbulence model is introduced to capture turbulence effects. The considered numerical tool is used to simulate the flow in a real 3D inducer in both non-cavitating and cavitating conditions.

2 Physical model and numerical method

The physical model considered in this work consists in the standard Navier-Stokes equations for a barotropic flow. Due to the barotropic equation of state (EOS) considered, the energy equation can be discarded since it is decoupled from the mass and momentum balances. Thus, considering a reference frame rotating with constant angular velocity ω, the following system of equations is obtained:

$$\frac{\partial \mathbf{W}}{\partial t} + \frac{\partial}{\partial x_j} F_j(\mathbf{W}) - \frac{\partial}{\partial x_j} \mu V_j(\mathbf{W}, \nabla \mathbf{W}) = \mathbf{S}(\omega, \mathbf{x}, \mathbf{W}) \tag{1}$$

In Eq. (1) the Einstein notation is used, μ is the molecular viscosity of the fluid, $\mathbf{W} = (\rho, \rho u_1, \rho u_2, \rho u_3)^T$ is the unknown vector, where ρ is the density and u_i the velocity component in the i^{th} direction. $\mathbf{F} = (F_1, F_2, F_3)$ and $\mathbf{V} = (V_1, V_2, V_3)$ are, respectively, the convective fluxes and the diffusive ones (not shown here for sake of brevity). Finally, $\mathbf{S}$ is the source term appearing in a frame of reference rotating with constant speed ω:

$$\begin{cases} \overline{\mathbf{S}} & = -\left(2\omega \wedge \rho\mathbf{u} + \rho\omega \wedge (\omega \wedge \mathbf{x})\right) \\ \mathbf{S}(\omega, \mathbf{x}, \mathbf{W}) & = \left(0,\ \overline{\mathbf{S}}^T\right)^T \end{cases} \tag{2}$$

System (1) is completely defined once a suitable constitutive equation $p = p(\rho)$ is introduced. In this work a weakly-compressible liquid at constant temperature T_L is considered as working fluid. The liquid density ρ is allowed to locally fall below the saturation limit $\rho_{Lsat} = \rho_{Lsat}(T_L)$ thus originating cavitation phenomena. A regime-dependent (wet/cavitating) constitutive relation is therefore adopted. As for the wet regime ($\rho \geq \rho_{Lsat}$), a barotropic model of the form

$$p = p_{sat} + \frac{1}{\beta_{sL}} \ln\left(\frac{\rho}{\rho_{Lsat}}\right) \tag{3}$$

is adopted, $p_{sat} = p_{sat}(T_L)$ and $\beta_{sL} = \beta_{sL}(T_L)$ being the saturation pressure and the liquid isentropic compressibility, respectively. As for the cavitating regime ($\rho < \rho_{Lsat}$), a homogeneous-flow model explicitly accounting for thermal cavitation effects and for the concentration of the active cavitation nuclei in the pure liquid has been adopted [1]:

$$\frac{p}{\rho}\frac{d\rho}{dp} = (1-\alpha)\left[(1-\varepsilon_L)\frac{p}{\rho_{Lsat}a_{Lsat}^2} + \varepsilon_L g^\star \left(\frac{p_c}{p}\right)^\eta\right] + \frac{\alpha}{\gamma_V} \tag{4}$$

where $g^\star$, η, γ_V and p_c are liquid parameters, a_{Lsat} is the liquid sound speed at saturation, $\alpha = 1 - \rho/\rho_{Lsat}$ and $\varepsilon_L = \varepsilon_L(\alpha, \zeta)$ is a given function (see [1] for its physical interpretation and for more details). The resulting unified barotropic state law for the liquid and for the cavitating mixture only depends on the two parameters T_L and ζ. For instance, for water at $T_L = 293.16K$, the other parameters involved in (3) and (4) are: $p_{sat} = 2806.82$ Pa, $\rho_{Lsat} = 997.29$ kg/m^3, $\beta_{sL} = 5\,10^{-10}$ Pa^{-1}, $g^* = 1.67$, $\eta = 0.73$, $\gamma_V = 1.28$, $p_c = 2.21\,10^7$ Pa and $a_{Lsat} = 1415$ m/s [6]. Note that despite the model simplifications leading to a unified barotropic state law, the transition between wet and cavitating regimes is extremely abrupt. Indeed, the sound speed falls from values of order 10^3 m/s in the pure liquid down to values of order 0.1 or 1 m/s in the mixture. The corresponding Mach number variation renders this state law very stiff from a numerical viewpoint. As for the definition of the molecular viscosity, a simple model, which is linear in the cavitating regime, is considered:

$$\mu(\rho) = \begin{cases} \mu_L & \text{if} \quad \rho \geq \rho_{Lsat} \\ \mu_v & \text{if} \quad \rho \leq \rho_v \\ \alpha\mu_v + (1-\alpha)\mu_L & \text{otherwise} \end{cases} \tag{5}$$

in which μ_v and μ_L are the molecular viscosity of the vapor and of the liquid respectively, which, consistently with the assumptions made in the adopted cavitation model, are considered constant and computed at $T = T_L$.

The spatial discretization of the governing equations is based on a mixed finite-element/finite-volume formulation on unstructured grids. Starting from an unstructured tetrahedral grid, a dual finite-volume tessellation is obtained by the rule of medians. The semi-discrete balance applied to cell C_i reads (not accounting for boundary contributions):

$$V_i \frac{d\mathbf{W}_i}{dt} + \sum_{j \in N(i)} \Phi_{ij} + \Upsilon_i = \Omega_i \tag{6}$$

where $\mathbf{W}_i$ is the semi-discrete unknown associated with C_i, V_i is the cell volume, and $N(i)$ represents the set of neighbors of the i^{th} cell. The numerical discretization of the convective flux crossing the boundary ∂C_{ij} shared by C_i and C_j (positive towards C_j) is denoted Φ_{ij}, while Υ_i and Ω_i are the numerical discretizations for, respectively, the viscous fluxes and the source term. Let us describe, first, the first-order version of the used numerical method. Once defined $\mathbf{n}_{ij} = \left(n_{ij,1}, n_{ij,2}, n_{ij,3}\right)^T$

as the integral over ∂C_{ij} of the outer unit normal to the cell boundary, it is possible to approximate Φ_{ij} by the following preconditioned flux function:

$$\Phi_{ij} = \frac{n_{ij,k}\left(F_k(\mathbf{W}_i) + F_k(\mathbf{W}_j)\right)}{2} - \frac{1}{2}\begin{pmatrix} \lambda_1^p & 0 & 0 & 0 \\ 0 & \left(\Delta^{32}\lambda^p\right) n_{ij,1}^2 + \lambda_3^p & \left(\Delta^{32}\lambda^p\right) n_{ij,1}n_{ij,2} & \left(\Delta^{32}\lambda^p\right) n_{ij,1}n_{ij,3} \\ 0 & \left(\Delta^{32}\lambda^p\right) n_{ij,2}n_{ij,1} & \left(\Delta^{32}\lambda^p\right) n_{ij,2}^2 + \lambda_3^p & \left(\Delta^{32}\lambda^p\right) n_{ij,2}n_{ij,3} \\ 0 & \left(\Delta^{32}\lambda^p\right) n_{ij,3}n_{ij,1} & \left(\Delta^{32}\lambda^p\right) n_{ij,3}n_{ij,2} & \left(\Delta^{32}\lambda^p\right) n_{ij,3}^2 + \lambda_3^p \end{pmatrix} (\mathbf{W}_j - \mathbf{W}_i) \tag{7}$$

where $\Delta^{32}\lambda^p = \lambda_2^p - \lambda_3^p$, $\lambda_1^p = \theta^{-1}\lambda_{ij}$, $\lambda_2^p = \theta\lambda_{ij}$, $\lambda_3^p = \lambda_{ij}$ and the parameters θ and λ_{ij} are defined as follows:

$$\theta = \theta(M) = \begin{cases} 10^{-6} & \text{if } M \leq 10^{-6} \\ \min(M,1) & \text{otherwise} \end{cases}, \quad M = \frac{|\tilde{\mathbf{u}}_{ij}|}{\tilde{a}_{ij}}, \quad \lambda_{ij} = \tilde{\mathbf{u}}_{ij} + \tilde{a}_{ij} \tag{8}$$

$\tilde{\mathbf{u}}_{ij}$ and $\tilde{a}_{ij}$ being the Roe averages for, respectively, the velocity and the sound of speed. The discretization (7) is the 3D extension of LD-HLL scheme defined in [2] as a low diffusive modification of the Rusanov scheme.

The discretization of the viscous fluxes is instead based on P1 finite-elements in which the test functions are linear functions on the tetrahedral element. The source term is discretized as follows:

$$\Omega_i := \begin{pmatrix} 0 \\ -2\,\omega \wedge \rho_i \mathbf{u}_i + \rho_i\,\mathbf{r}_i \end{pmatrix} \quad \mathbf{r}_i := -\,\omega \wedge (\omega \wedge \mathbf{g}_i) \tag{9}$$

$\mathbf{g}_i$ being the centroid of the i^{th} cell.

A first-order implicit Euler method can be used for time-advancing. As a consequence, at each time step it is necessary to compute $\mathscr{F}_i^{n+1} = \mathscr{F}(\mathbf{W}_j^{n+1}, j \in \bar{N}(i))$, where $\bar{N}(i) = N(i) \cup \{i\}$ and $\mathscr{F}_i$ is defined as $\mathscr{F}_i = \sum_{j \in N(i)} \Phi_{ij} + \Upsilon_i - \Omega_i$.

In order to avoid the direct solution of large non-linear system of equations at each time step a linearization can be performed finding an approximation of $\mathscr{F}_i^{n+1}$ in the form:

$$\Delta^n \mathscr{F}_i \simeq \sum_{j \in \bar{N}(i)} D_{ij}\,\Delta^n \mathbf{W}_j \tag{10}$$

where $\Delta^n(\cdot) = (\cdot)^{n+1} - (\cdot)^n$. Using this approximation, the following linear system must be solved at each time step:

$$|V_i| \frac{\mathbf{W}_i^{n+1} - \mathbf{W}_i^n}{\Delta t} + \sum_{j \in \bar{N}(i)} D_{ij}\,\Delta^n \mathbf{W}_j = -\mathscr{F}(\mathbf{W}_j^n, j \in \bar{N}(i)) \tag{11}$$

The implicit linearized scheme is completely defined once a suitable definition for the matrices D_{ij} is given. Since viscous and source terms are easily differentiable, the use of the Jacobian matrices has been considered here to compute their contribution to D_{ij}. However the computation of the Jacobian matrices can be more challenging for the convective fluxes. Thus, in this work the approximate linearization developed in [2] for the numerical flux function (7) has been used. Once matrices D_{ij} are given, the first-order numerical method (11) is completely defined.

Since viscous and source terms are already second-order accurate in space, the extension to second-order accuracy in space can be achieved by simply using a classical MUSCL technique [4], in which the convective fluxes are computed by using extrapolated values at the cell interfaces. The second-order accuracy in time is then achieved through the use of a backward differentiation formula. However, the linearization for the second-order accurate fluxes and the solution of the resulting linear system imply significant computational costs and memory requirements. Thus, a defect-correction technique [5] is used here. It consists in iteratively solving simpler problems obtained just considering the same linearization as used for the first-order scheme. The number of DeC iterations r is typically chosen equal to 2. Indeed, it can be shown [5] that only one defect-correction iteration is theoretically needed to reach a second-order accuracy while few additional iterations (one or two) can improve the robustness.

Finally, in order to account for the turbulence effects the RANS approach together with the standard turbulence model $k - \varepsilon$ have been used. For the sake of brevity the additional terms introduced in the system of equation by this model are not shown. We just mention that the convective and viscous turbulent fluxes are discretized using the same methods considered for their laminar counterparts. Similarly, the turbulent source term appearing in the equations for k and ε is discretized using the same approach considered for the source term associated to the rotating frame of reference.

3 Numerical experiments

In this section the numerical tool described in Sect. 1 is applied to the simulations of the flow in a real three blade axial inducer [6]. It is a three blade inducer with a tip blade radius of 81 mm and 2 mm radial clearance between the blade tip and the external case. Experimental data are available for all the numerical simulations described in the following. In particular the pressure jump between two different stations has been measured for a wide range of working conditions: from small to large mass flow rates, non-cavitating and cavitating conditions and different values of the rotational speed ω_z. The results are presented in terms of the mean adimensionalized pressure jump Ψ as a function of the adimensionalized discharge Φ:

$$\Psi = \frac{\Delta P}{\rho_L \omega_z^2 R_T^2} \qquad \Phi = \frac{Q}{\pi R_T^2 \omega_z R_T} \tag{12}$$

where Q is the discharge, R_T is the radius of the tip of blade, ρ_L the density of the liquid and ω_z is the angular velocity. Note that the numerical pressure jump is averaged over one complete revolution of the inducer. A cylindrical computational domain is used, whose external surface is coincident with the inducer case. The inlet is placed 249 mm ahead of the inducer nose and the outlet is placed 409 mm behind. A second computational domain, characterized by a larger streamwise length (the inlet 1120 mm ahead the inducer nose) has also been considered. Two different grids have been generated to discretize the shorter domain: the basic one G1 (1926773 cells) and G2 (3431721 cells) obtained from G1 by refining the region between the blade tip and the external case. In particular, inside the tip clearance region there are $3-4$ nodes for the grid G1, while there are $9-10$ points for G2. The larger domain has been discretized by grid G1L (2093770 cells), which coincides with G1 in the original domain. The working conditions considered in this work are shown in Table 1, where p_{out} is the outlet pressure of the flow and $\sigma = \dfrac{p - p_{Lsat}}{0.5\rho\omega_z^2 R_T^2}$ is the cavitating number (only shown for cavitating simulations). Note that, except when differently stated, the simulations do not include turbulence effects.

Table 1 Conditions of the numerical simulations and of the experiments

Benchmark	Ind1	Ind2	Ind3	Ind4	Ind5	Ind6
Φ	0.0584	0.0391	0.0185	0.0531	0.0531	0.0531
ω_z (rpm)	1500	1500	1500	3000	3000	3000
p_{out} (Pa)	125000	125000	125000	60000	85000	82500
T (C°)	25°	25°	25°	16.8°	16.8°	16.8°
σ	-	-	-	0.056	0.084	0.077

As shown in Table 1, all the simulations in non cavitating conditions use the same rotational velocity of 1500 rpm. In the $\Phi - \Psi$ plane the experimental curves of the performances of the inducer are roughly independent from the rotational velocity ω_z [6]. As a consequence, validating the numerical tool for a specific rotational velocity and different flow rates should validate the proposed numerical tool for a generic rotational velocity. Table 2 shows the results for the non-cavitating simulations. It clearly appears that the lower is the discharge Φ, the worse are the results. Already with the coarsest grid G1, rather satisfactory results are obtained for intermediate and high discharge values, Ind2 and Ind1, respectively. Furthermore the quantitative agreement is further improved considering the more refined grid G2 for the case Ind2. Conversely, for the low discharge case, Ind3, the simulations with the grid G1 and G2 greatly overestimate the pressure jump by, respectively, 41% and 30%. The magnitude of this error could be ascribed to the backward flow between the inducer blades and the external case. The correct resolution of this flow is of crucial importance for the determination of the performance of an inducer. Since the smaller is the mass flow rate the greater is the backflow, we investigated

Table 2 Pressure jump in non-cavitating conditions

	Experimental Ψ	Numerical Ψ	Error%
G1-Ind1	0.122	0.114	−6.6%
G1-Ind2	0.186	0.204	+9.7%
G2-Ind2	0.186	0.179	−3.8%
G1-Ind3	0.214	0.302	+41%
G2-Ind3	0.214	0.278	+30%
G1L-Ind3	0.214	0.297	+39%
G1L-Ind3-T	0.214	0.239	+12%

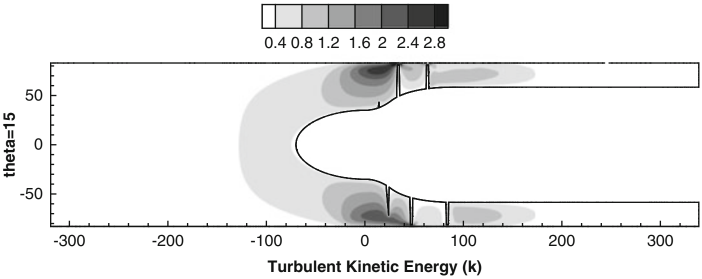

Fig. 1 Cross section of the averaged k field at $\theta = 15°$, simulation G1L-Ind3 (view of the shorter domain)

two possible explanations of this behavior. The first one was that the distance of the inlet from the inducer nose was not large enough to avoid spurious effects on the solution, the second one was that for this case turbulence effects have to be included. The results of the first simulations for the longer computational domain, G1L-Ind3, show that even if there is a small effect, a decrease from 41% to 39%, this is not the source of the error. Instead the results of the simulation G1L-Ind3-T, i.e. the one done considering the RANS model, show that in this case turbulence is a key-issue. Indeed, in this case the error falls down to 12%, less than the error obtained with the refined grid G2 in laminar conditions. As expected the effects of turbulence are particularly important near the gap between the blades and the external case, as it is shown by Fig. 1 by considering the isocontours of k. This strongly affects the backflow and, thus, the pressure jump. This also explains why for larger flow rates, for which the backflow is less important, the effects of turbulence are not so strong and a good agreement with experimental data can be obtained also in laminar simulations.

The mass flow rate for the cavitating cases is large enough to prevent the issues related to the backflow previously described, thus only laminar simulations are considered. The results for the cavitating conditions, reported in Table 3, show that the first grid G1 is not enough refined to correctly describe cavitation for this case. The pressure jump is greatly overestimated. For these conditions the error is related to the underestimation of the cavitating region: the experimental data for $\sigma = 0.056$ show a large cavitating zone and consequently the performance of the

Table 3 Numerical results for the cavitating simulations

	Experimental Ψ	Numerical Ψ	Error%
G1-Ind4	0.105	0.143	$+36\%$
G2-Ind5	0.143	0.130	-8.9%
G2-Ind6	0.137	0.130	-5.0%

Fig. 2 Isocontours of the cavitating region, $\alpha = 0.005$, for the simulation G2-Ind6

inducer is significantly deteriorated. Instead, in the simulation with grid G1 the extension of the cavitating region is greatly underestimated and, as a consequence, the "numerical" performance of the inducer is similar to the non cavitating case. Grid refinement is particularly effective as shown by the results for the simulations, G2-Ind5 and G2-Ind6. The error in the prediction of the pressure jump is reduced and the extension of the cavitating region, even if it is still underestimated, is closer to the one found in experiments, as it is shown by Fig. 2 which plots the isocontours of the void fraction, corresponding to the cavitating region. Note that when the coarse grid G1 is used the cases Ind5 and Ind6 are not cavitating.

Acknowledgements The support of the European Space Agency under Contract number 20081/06/NL/IA is gratefully acknowledged. The authors also wish to thank the Italian Computer Center CASPUR for having provided computational resources and support.

References

1. L. d'Agostino, E. Rapposelli, C. Pascarella, A. Ciucci *A Modified Bubbly Isenthalpic Model for Numerical Simulation of Cavitating Flows.* 37th AIAA/ASME/SAE/ASEE Joint Propulsion Conference, Salt Lake City, UT, USA, 2001.

2. M. Bilanceri, F. Beux, M.V. Salvetti *An Implicit Low-Diffusive HLL Scheme with Complete Time Linearization: Application to Cavitating Barotropic Flows.* Computer & Fluids, 39(10):1990–2006, 2010.
3. S. Camarri, M.V. Salvetti, B. Koobus, A. Dervieux. *A low-diffusion MUSCL scheme for LES on unstructured grids.* Computers & Fluids, 33:1101–1129, 2004.
4. B. van Leer. *Towards the ultimate conservative difference scheme* V*: a second-order sequel to* G*odunov's method.* J. Comput. Phys., 32(1):101–136, 1979.
5. R. Martin, H. Guillard. *A second order defect correction scheme for unsteady problems.* Computers & Fluids, 25(1):9–27, 1996.
6. L. Torre, G. Pace, P. Miloro, A. Pasini, A. Cervone, L. d'Agostino, *Flow Instabilities on a Three Bladed Axial Inducer at Variable Tip Clearance.* 13^{th} International Symposium on Transport Phenomena and Dynamics of Rotating Machinery, Honolulu, Hawaii, USA.

The paper is in final form and no similar paper has been or is being submitted elsewhere.